

Article

MSVR & Operator-Based System Design of Intelligent MIMO Sensorless Control for Microreactor Devices

Tatsuma Kato, Kosuke Nishizawa and Mingcong Deng * 

Department of Electrical and Electronic Engineering, Graduate School of Engineering,
Tokyo University of Agriculture and Technology, 2-24-16 Nakacho, Koganei-shi 184-8588, Tokyo, Japan
* Correspondence: deng@cc.tuat.ac.jp

Abstract: Recently, microreactors, which are tubular reactors capable of fast and highly efficient chemical reactions, have attracted attention. However, precise temperature control is required because temperature changes due to reaction heat can cause reactions to proceed differently from those designed. In a previous study, a single-input/output nonlinear control system was proposed using a model in which the microreactor is divided into three regions and the thermal equation is formulated considering the temperature gradient, but it could not control two different temperatures. In this paper, a multi-input, multi-output nonlinear control system was designed using operator theory. On the other hand, when the number of parallel microreactors is increased, a sensorless control method using M-SVR with a generalized Gaussian kernel was incorporated into the MIMO nonlinear control system from the viewpoint of cost reduction, and the effectiveness of the proposed method was confirmed via experimental results.

Keywords: nonlinear control; microreactor; Peltier device; operator theory; multi-output support vector regression; generalized Gaussian kernel



Citation: Kato, T.; Nishizawa, K.; Deng, M. MSVR & Operator-Based System Design of Intelligent MIMO Sensorless Control for Microreactor Devices. *Computation* **2024**, *12*, 2. <https://doi.org/10.3390/computation12010002>

Academic Editor: Xiaoyuan Luo

Received: 30 October 2023

Revised: 29 November 2023

Accepted: 13 December 2023

Published: 25 December 2023



Copyright: © 2023 by the authors. Licensee MDPI, Basel, Switzerland. This article is an open access article distributed under the terms and conditions of the Creative Commons Attribution (CC BY) license (<https://creativecommons.org/licenses/by/4.0/>).

1. Introduction

A microreactor is a tube-type reactor with a reaction capacity of about microliters. The advantages of microreactors include the ability to achieve fast and highly efficient chemical reactions due to the large surface area per unit volume and the ability to safely handle chemical reactions that may cause explosions or generate hazardous substances because the reaction volume is much smaller than that of batch reaction systems. On the other hand, precise temperature control is essential because temperature changes due to the heat of chemical reactions can cause chemical reactions that are not intended in the design. In this study, a Peltier element, one of the thermoelectric conversion elements, is used to achieve vibration-free and precise temperature control. Peltier elements have the property of heat pumps, in which a high-temperature surface and a low-temperature surface are generated when an electric current is applied, and heat is transferred from the low-temperature surface to the high-temperature surface [1,2].

The Peltier elements, microreactors, and heat spreaders used in this study, which are cooling auxiliary mechanisms, have uncertainties due to the difficulty of accurately describing their models, and therefore must be controlled to account for them. To solve this problem, research [3] on methods for the robust design of parallel compensators for non-ASPR plants with structured uncertainties has been conducted. While sliding mode control is well known as a nonlinear control theory [4–7], this study uses operator theory, which can design robust and stable controllers for nonlinear systems [8,9]. As a study using operator theory, a nonlinear temperature control system has been designed for an aluminum plate with a Peltier device that has uncertainty [10]. In recent years, due to the popularity of AI research [11–19], research combining operator theory and AI has also been conducted. In addition, research on multi-input/output systems, such as research on

a two-dimensional direction-of-arrival estimation using a polarization rectangular array under multipath propagation [20], has attracted much attention and has been actively studied in operator theory. As an example of combined research, a study on the multi-input/output tip position control of a 3-DOF soft actuator with uncertainty proposes a method of uncertainty compensation using M-SVR, a type of machine learning, and the control of multi-input/output systems using operator theory [21]. Operator theory has also been applied to a variety of other control objects [22–25].

In addition, the output estimates of observers designed using uncertain models deviate significantly from the real values due to modeling errors. Therefore, a study on a real-time estimation filter robust to the viscoelasticity of articulated arms in motion has been reported by considering and quantitatively evaluating an uncertain articulated arm viscoelasticity model with measurement error [26]. It was also extended to a practical filter algorithm for estimating the articulated viscoelasticity of human arms using a generalized Gaussian distribution [27].

Based on the above, the objectives of this study are twofold. The first is to realize a multi-input/output temperature control system to enable control of two temperatures within a microreactor. The second is to realize sensorless control in order to solve the increase in the number of sensors caused by numbering-up (a production method in which the number of microreactors is increased and parallelized in order to achieve mass production). Since the model of microreactors includes uncertainty, a machine learning model, M-SVR, is used as an estimator in this study. M-SVR is a machine learning method that extends SVR, which is a multiple-input, single-output method, to multiple outputs. M-SVR can consider effects among outputs compared with general SVR, and M-SVR has the advantage that the number of hyperparameters does not increase as the number of outputs increases [28,29]. Furthermore, to obtain higher generalization performance than the RBF kernel in offline learning, we design a sensorless control system with a model using a generalized Gaussian kernel. On the other hand, since the generalized Gaussian kernel increases the number of parameters to be tuned compared with the RBF kernel and makes it difficult to tune to the optimal parameters, a real-coded genetic algorithm [30,31] is used for parameter tuning to efficiently search for the optimal parameters. The effectiveness of these results is confirmed via simulations and experiments on actual equipment.

This section describes the structure of this paper. Section 2 describes the experimental apparatus used in this study, its mathematical modeling, and modeling using M-SVR. Section 3 describes the design of the multi-input multi-output temperature control system and the sensorless control system using M-SVR, based on the modeling in Section 2. Section 4 describes the results of the simulation and actual machine experiments using the control system designed in Section 3, verifies the effectiveness of the proposed method, and concludes in Section sec:conclusion.

2. Modeling

As shown in Figure 1, the microreactor and heat spreader are modeled by dividing them into three regions and formulating the thermal equations for each. Let Part A_1 , Part A_2 , and Part A_3 be the areas to the left of the heat spreader and Part W_1 , Part W_2 , and Part W_3 be the areas to the left of the microreactor, where S_n represents the area, and the values are shown in Table 1. The parameters used for modeling are shown in Table 2. Here, Peltier elements are installed on both sides of Part A_1 and Part A_3 .

Table 1. Parameters of area.

Symbol	Value	Unit	Symbol	Value	Unit
S_1	2.6×10^{-3}	m^2	S_2	7.0×10^{-4}	m^2
S_3	9.8×10^{-3}	m^2	S_4	9.0×10^{-4}	m^2
S_5	$9.0\pi \times 10^{-6}$	m^2	S_6	$3.0\pi \times 10^{-4}$	m^2
S_7	1.4×10^{-3}	m^2	S_8	2.8×10^{-4}	m^2
S_9	$1.2\pi \times 10^{-4}$	m^2			

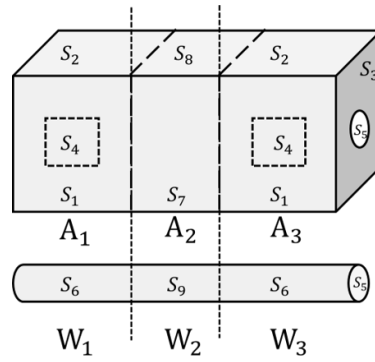


Figure 1. Model of microreactor and heat spreader.

Table 2. Parameters of microreactor.

Symbol	Description	Value	Unit
T_0	Initial temperature	-	[K]
T_{a_n}	Aluminum temperature ($n = 1, 2, 3$)	-	[K]
T_{w_k}	Water temperature ($k = 1, 2, 3$)	-	[K]
y_{a_n}	Aluminum cooling temperature	-	[K]
y_{w_k}	Water cooling temperature	-	[K]
u_{d_1}, u_{d_2}	Heat absorption from Peltier element	-	[W]
c_a	Specific heat of aluminum	468	J/(kg · K)
c_w	Specific heat of water	2174.64	J/(kg · K)
λ_a	Thermal conductivity of aluminum	238	J/(kg · K)
λ_w	Thermal conductivity of water	0.602	J/(kg · K)
α	Heat transfer coefficient of air	180	W/(m ² · K ⁴)
α_w	Heat transfer coefficient of water	500	W/(m ² · K ⁴)
m_{a_1}, m_{a_3}	Mass of HS	1.31	kg
m_{a_2}	Mass of HS	0.52	kg
m_{w_1}, m_{w_3}	Mass of Water	1.41×10^{-3}	kg
m_{w_2}	Mass of Water	0.6×10^{-3}	kg
σ	Stefan–Boltzmann constant	5.67×10^{-8}	W/(m ² · K ⁴)
ϵ_a	Thermal emissivity of aluminum	0.2	-
ϵ_w	Thermal emissivity of water	0.93	-

2.1. Modeling of Heat Spreader

This section models heat spreaders.

$$\begin{aligned}
 \text{Part A}_1 : \frac{d(T_0 - T_{a_1})m_{a_1}c_a}{dt} = & 2u_{d_1} - \alpha(T_0 - T_{a_1})(2S_1 + 2S_2 + S_3 - S_5) \\
 & + \alpha_w S_6(T_{a_1} - T_{w_1}) + \frac{\lambda_a S_3(T_{a_1} - T_{a_2})}{dx} \\
 & + \epsilon_a \sigma (T_{a_1}^4 - T_0^4)(2S_1 + 2S_2 + S_3 - S_5)
 \end{aligned} \tag{1}$$

$$\begin{aligned} \text{Part A}_2 : \frac{d(T_0 - T_{a_2})m_{a_2}c_a}{dt} &= -\alpha(T_0 - T_{a_2})(2S_7 + 2S_8) + \alpha_w S_9(T_{a_2} - T_{w_2}) \\ &\quad - \frac{\lambda_a S_3(T_{a_1} - T_{a_2})}{dx} - \frac{\lambda_a S_3(T_{a_3} - T_{a_2})}{dx} \\ &\quad + \epsilon_a \sigma(T_{a_2}^4 - T_0^4)(2S_7 + 2S_8) \end{aligned} \tag{2}$$

$$\begin{aligned} \text{Part A}_3 : \frac{d(T_0 - T_{a_3})m_{a_3}c_a}{dt} &= 2u_{d_2} - \alpha(T_0 - T_{a_3})(2S_1 + 2S_2 + S_3 - S_5) \\ &\quad + \alpha_w S_6(T_{a_3} - T_{w_3}) + \frac{\lambda_a S_3(T_{a_3} - T_{a_2})}{dx} \\ &\quad + \epsilon_a \sigma(T_{a_3}^4 - T_0^4)(2S_1 + 2S_2 + S_3 - S_5) \end{aligned} \tag{3}$$

If the variables are defined as $y_{a_n} = T_0 - T_{a_n}$ ($n = 1, 2, 3$), Part A_n can be expressed by Equations (4)–(6).

$$\text{Part A}_1 : \frac{dy_{a_1}}{dt} = \omega_{a_1} + A_{a_{11}}y_{a_1} + A_{a_{12}}y_{a_1}^2 + A_{a_{13}}y_{a_1}^3 + A_{a_{14}}y_{a_1}^4 + \frac{\lambda_a S_3 y_{a_2}}{m_{a_1} c_a dx} \tag{4}$$

$$\text{Part A}_2 : \frac{dy_{a_2}}{dt} = \omega_{a_2} + A_{a_{21}}y_{a_2} + A_{a_{22}}y_{a_2}^2 + A_{a_{23}}y_{a_2}^3 + A_{a_{24}}y_{a_2}^4 - \frac{\lambda_a S_3 (y_{a_1} + y_{a_3})}{m_{a_2} c_a dx} \tag{5}$$

$$\text{Part A}_3 : \frac{dy_{a_3}}{dt} = \omega_{a_3} + A_{a_{31}}y_{a_3} + A_{a_{32}}y_{a_3}^2 + A_{a_{33}}y_{a_3}^3 + A_{a_{34}}y_{a_3}^4 + \frac{\lambda_a S_3 y_{a_2}}{m_{a_3} c_a dx} \tag{6}$$

In this case, ω_{a_n} are as follows:

$$\omega_{a_1} = \frac{2u_{d_1} + \alpha_w S_6 y_{w_1}}{m_{a_1} c_a}, \omega_{a_2} = \frac{\alpha_w S_9 y_{w_2}}{m_{a_2} c_a}, \omega_{a_3} = \frac{2u_{d_1} + \alpha_w S_6 y_{w_3}}{m_{a_3} c_a}$$

And $A_{a_{nm}}$ are as follows:

$$\begin{aligned} A_{a_{11}} &= \frac{(\alpha + 4\epsilon_a \sigma T_0^3)(S_1 + S_2 + S_3 - 2S_4 - S_5) + \alpha_w S_6 + \frac{\lambda_a S_3}{dx}}{m_{a_1} c_a}, \\ A_{a_{12}} &= \frac{6\epsilon_a \sigma T_0^2 (S_1 + S_2 + S_3 - 2S_4 - S_5)}{m_{a_1} c_a}, \\ A_{a_{13}} &= \frac{4\epsilon_a \sigma T_0 (S_1 + S_2 + S_3 - 2S_4 - S_5)}{m_{a_1} c_a}, \\ A_{a_{14}} &= \frac{\epsilon_a \sigma (S_1 + S_2 + S_3 - 2S_4 - S_5)}{m_{a_1} c_a}, \\ A_{a_{21}} &= \frac{(\alpha + 4\epsilon_a \sigma T_0^3)(2S_7 + 2S_8) + \alpha_w S_9 + \frac{2\lambda_a S_3}{dx}}{m_{a_2} c_a}, \\ A_{a_{22}} &= \frac{6\epsilon_a \sigma T_0^2 (2S_7 + 2S_8)}{m_{a_2} c_a}, \\ A_{a_{23}} &= \frac{4\epsilon_a \sigma T_0 (2S_7 + 2S_8)}{m_{a_2} c_a}, \\ A_{a_{24}} &= \frac{\epsilon_a \sigma (2S_7 + 2S_8)}{m_{a_2} c_a}, \\ A_{a_{31}} &= \frac{(\alpha + 4\epsilon_a \sigma T_0^3)(S_1 + S_2 + S_3 - 2S_4 - S_5) + \alpha_w S_6 + \frac{\lambda_a S_3}{dx}}{m_{a_3} c_a}, \end{aligned}$$

$$A_{a32} = \frac{6\epsilon_a\sigma T_0^2(S_1 + S_2 + S_3 - 2S_4 - S_5)}{m_{a3}c_a},$$

$$A_{a33} = \frac{4\epsilon_a\sigma T_0(S_1 + S_2 + S_3 - 2S_4 - S_5)}{m_{a3}c_a},$$

$$A_{a34} = \frac{\epsilon_a\sigma(S_1 + S_2 + S_3 - 2S_4 - S_5)}{m_{a3}c_a}$$

2.2. Modeling of Microreactor

In this section, we model the tubes.

$$\text{Part W}_1 : \frac{d(T_0 - T_{\omega_1})m_{\omega}c_{\omega}}{dt} = - \frac{\lambda_{\omega}S_5((T_{\omega_0} - T_{\omega_1}) - (T_{\omega_0} - T_{\omega_2}))}{dx} + \alpha_{\omega}S_6(T_{\omega_1} - T_{a_1}) \tag{7}$$

$$\text{Part W}_2 : \frac{d(T_0 - T_{\omega_2})m_{\omega}c_{\omega}}{dt} = - \frac{\lambda_{\omega}S_5(2(T_{\omega_0} - T_{\omega_2}) - (T_{\omega_0} - T_{\omega_1}) - (T_{\omega_0} - T_{\omega_3}))}{dx} + \alpha_{\omega}S_9(T_{\omega_2} - T_{a_2}) \tag{8}$$

$$\text{Part W}_3 : \frac{d(T_0 - T_{\omega_3})m_{\omega}c_{\omega}}{dt} = - \frac{\lambda_{\omega}S_5((T_{\omega_0} - T_{\omega_3}) - (T_{\omega_0} - T_{\omega_2}))}{dx} + \alpha_{\omega}S_6(T_{\omega_3} - T_{a_3}) \tag{9}$$

If the variables are defined as $y_{w_k} = T_0 - T_{w_k} (k = 1, 2, 3,)$, Part W_k can be expressed by Equations (10)–(12).

$$\text{Part W}_1 : \frac{dy_{w_1}}{dt} = \omega_{w_1} - A_{w_1}y_{w_1} + \frac{\lambda_{\omega}S_5y_{w_2}}{m_{w_1}c_w dx} \tag{10}$$

$$\text{Part W}_2 : \frac{dy_{w_2}}{dt} = \omega_{w_2} - A_{w_2}y_{w_2} + \frac{\lambda_{\omega}S_5(y_{w_1} + y_{w_3})}{m_{w_2}c_w dx} \tag{11}$$

$$\text{Part W}_3 : \frac{dy_{w_3}}{dt} = \omega_{w_3} - A_{w_3}y_{w_3} + \frac{\lambda_{\omega}S_5y_{w_2}}{w_3c_w dx} \tag{12}$$

In this case, ω_{w_k} and $A_{a_{wk}}$ are as follows:

$$\omega_{w_1} = \frac{\alpha_w S_6 y_{a_1}}{m_{w_1} c_w}, \quad \omega_{w_2} = \frac{\alpha_w S_9 y_{a_2}}{m_{w_2} c_w}, \quad \omega_{w_3} = \frac{\alpha_w S_6 y_{a_3}}{m_{w_3} c_w} \tag{13}$$

$$A_{w_1} = \frac{\frac{\lambda_w S_5}{dx} + \alpha_w S_6}{m_{w_1} c_w}, \quad A_{w_2} = \frac{\frac{\lambda_w S_5}{dx} + \alpha_w S_9}{m_{w_2} c_w}, \quad A_{w_3} = \frac{\frac{\lambda_w S_5}{dx} + \alpha_w S_6}{m_{w_3} c_w} \tag{14}$$

2.3. Modeling via M-SVR

To estimate the temperature of a microreactor, this section uses training data to build a model using M-SVR. M-SVR is a machine learning method that extends SVR to multiple outputs and has the advantage over general SVR of being able to consider the effects between outputs. Another advantage is that the number of hyperparameters does not increase as the number of outputs increases [28,29]. The theory of M-SVR is presented in Appendix B. In this study, a generalized Gaussian kernel is used to achieve higher generalization performance than the RBF kernel. The generalized Gaussian kernel is a kernel based on the generalized Gaussian distribution and has the property of changing the shape of the distribution with the value of the shape parameter [26]. The theory of generalized Gaussian kernels is presented in Appendix C. Three features, the currents i_1 and i_2 flowing in the Peltier element and T_{a_2} , the temperature of aluminium, are used as training data for the input of M-SVR, and five features, T_{w_1} , T_{a_1} , and T_{a_3} , the temperature of the microreactor, and T_{a_1} and T_{a_2} , the temperature of aluminium, are used as training data for the output. The training data are obtained by applying a constant current to

currents i_1 and i_2 in 15 combinations obtained from 0, 100, 200, and 400 mA for 500 s each to obtain the temperatures T_{w_1} , T_{w_2} , and T_{w_3} of the microreactor and T_{a_1} , T_{a_2} , and T_{a_3} of the aluminium. The 100 samples of data obtained from each current combination were summed to obtain 1500 samples of data, which were used as training data to create the model. Hyperparameter optimization using a real-coded genetic algorithm [30] with 50 generations and 20 individuals, ranking selection as the selection method, and SPX crossover [31] as the crossover method, using the training data obtained in the experiment, and manually adjusted results are shown in Tables 3 and 4, and MSE values in Table 5. Note that the manual adjustment is a trial-and-error adjustment made to obtain a good evaluation value using the parameters obtained by the real-valued genetic algorithm as a base point. The results show that the generalized Gaussian kernel is more accurate than the RBF kernel, so the M-SVR model with the generalized Gaussian kernel is used in this study.

Table 3. Parameters of RBF.

Symbol	Description	Value
C	Regularization parameter	106.8
ϵ	Insensitive factor	0.0077
γ	Kernel coefficient for RBF	0.371

Table 4. Parameters of generalized Gaussian kernel.

Symbol	Description	Value
C	Regularization parameter	251.96
ϵ	Insensitive factor	6.32×10^{-4}
γ	Shape parameter	0.5151
σ	Standard deviation	48.007

Table 5. MSE comparison.

Description	PartW ₁	PartW ₂	PartW ₃	PartA ₁	PartA ₃
RBF	0.0020	0.0015	0.0015	0.0016	0.0015
GGD	0.0015	0.0010	0.0011	0.0011	0.0011

3. Control Design

When performing MIMO temperature control, it is necessary to consider the coupling elements that occur between each control system. In this study, the coupling elements are separated based on the literature [8], and the two-input, two-output control system is divided into two independent subsystems for control. The theory is described in Appendix A.

3.1. Right Factorization

Using the model derived in Sections 2.1 and 2.2, we perform a right factorization based on operator theory. First, from Equations (4)–(6) and (10)–(12), we have that

$$\omega_{a_n} = \frac{z_{a_n}}{m_{a_n}c_a}, \omega_{w_k} = \frac{z_{w_k}}{m_{w_k}c_w} \tag{15}$$

$$\text{Part A}_n : \dot{y}_{a_n} = \frac{z_{a_n}}{m_{a_n}c_a} - A_{a_{n1}}y_{a_n} + A_{a_{n2}}y_{a_n}^2 - A_{a_{n3}}y_{a_n}^3 + A_{a_{n4}}y_{a_n}^4 \tag{16}$$

$$\text{Part W}_k : \dot{y}_{w_k} = \frac{z_{w_k}}{m_{w_k}c_w} - A_{w_k}y_{w_k} \tag{17}$$

is expressed as follows.

In this case, z_{a_n} and z_{w_k} are the input signals of processes P_{A_n} and P_{W_k} , respectively. In addition, y_{a_n} and y_{w_k} are the outputs of processes P_{A_n} and P_{W_k} , respectively. Here, z_{a_n} and z_{w_k} are expressed as follows.

$$z_{a_n} = \begin{cases} 2u_{d_1} + G_a y_{a_2} + G_{aw} y_{w_1} & (n = 1) \\ G_a y_{a_1} + G_a y_{a_3} + G_{aw_2} y_{w_2} & (n = 2) \\ 2u_{d_2} + G_a y_{a_2} + G_{aw} y_{w_3} & (n = 3) \end{cases} \quad (18)$$

$$z_{w_k} = \begin{cases} G_{aw} y_{a_1} + G_w y_{w_2} & (k = 1) \\ G_{aw_2} y_{a_2} + G_w (y_{w_1} + y_{w_3}) & (k = 2) \\ G_{aw} y_{a_3} + G_w y_{w_2} & (k = 3) \end{cases} \quad (19)$$

Note that $G_a, G_w, G_{aw}, G_{aw_2}, G_{sa},$ and G_{sw} are as follows.

$$\begin{aligned} G_a &= \frac{\lambda_a S_3}{dx}, & G_w &= \frac{\lambda_w S_5}{dx}, & G_{aw} &= \alpha_w S_6 \\ G_{aw_2} &= \alpha_w S_9, & G_{sa} &= \frac{2\lambda_a S_3}{dx}, & G_{sw} &= \frac{2\lambda_w S_5}{dx} \end{aligned} \quad (20)$$

The output-to-output coupling factors for each process are then as follows, where $H_a = \frac{\lambda_a S_3}{m_a c_a dx}, H_w = \frac{\lambda_w S_5}{m_w c_w dx}$.

$$\begin{aligned} H_{a_{12}} &= H_a y_{a_2}, & H_{a_{13}} &= 0, & H_{a_{21}} &= H_a y_{a_1} \\ H_{a_{23}} &= H_a y_{a_3}, & H_{a_{31}} &= 0, & H_{a_{32}} &= H_a y_{a_2} \end{aligned} \quad (21)$$

$$\begin{aligned} H_{w_{12}} &= H_w y_{a_2}, & H_{w_{13}} &= 0, & H_{w_{21}} &= H_w y_{a_1} \\ H_{w_{23}} &= H_w y_{a_3}, & H_{w_{31}} &= 0, & H_{w_{32}} &= H_w y_{a_2} \end{aligned} \quad (22)$$

The right factorization of each process is based on operator theory. Therefore, we represent each operator using a spatial representation as follows.

$$\begin{aligned} D_{a_n}^{-1} : z_{a_n}(t) &\rightarrow \omega_{a_n}(t) \\ &: \omega_{a_n} = \frac{z_{a_n}}{m_{a_n} c_a} \end{aligned} \quad (23)$$

$$\begin{aligned} N_{a_n} : \omega_{a_n}(t) &\rightarrow y_{a_n}(t) \\ &: \begin{cases} \dot{x}_{a_n} = \omega_{a_n} - A_{a_{n1}} y_{a_n} + A_{a_{n2}} y_{a_n}^2 - A_{a_{n3}} y_{a_n}^3 + A_{a_{n4}} y_{a_n}^4 \\ y_{a_n} = x_{a_n} \end{cases} \end{aligned} \quad (24)$$

3.2. Without Interference Effects

Figure 2 shows the control system for eliminating the effects of interference.

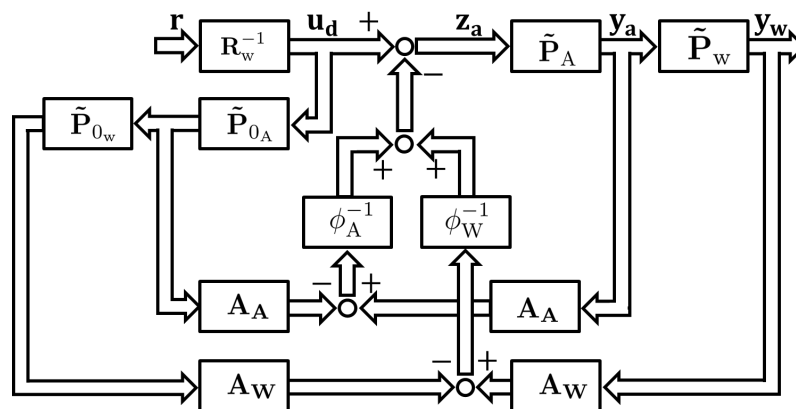


Figure 2. Without interference effects.

In this case, $\tilde{\mathbf{P}}_{\mathbf{A}} = (\tilde{P}_{A_1}, \tilde{P}_{A_2}, \dots, \tilde{P}_{A_n})$, $\tilde{P}_{A_n} = N_{A_n} R_{A_n}^{-1}$, $\tilde{\mathbf{P}}_{\mathbf{W}} = (\tilde{P}_{W_1}, \tilde{P}_{W_2}, \dots, \tilde{P}_{W_n})$, $\tilde{\mathbf{P}}_{0\mathbf{A}} = (\tilde{P}_{0A_1}, \tilde{P}_{0A_2}, \dots, \tilde{P}_{0A_n})$, and $\tilde{\mathbf{P}}_{0\mathbf{W}} = (\tilde{P}_{0W_1}, \tilde{P}_{0W_2}, \dots, \tilde{P}_{0W_n})$. $\tilde{\mathbf{P}}_{0\mathbf{A}}$ is the thermal model of the heat spreader, and $\tilde{\mathbf{P}}_{0\mathbf{W}}$ is the tube thermal model. $\tilde{\mathbf{P}}_{0\mathbf{A}}$ can undergo right factorization as follows.

$$\begin{aligned} \tilde{P}_{0A_n} &= N_{A_n} R_{A_n}^{-1} \\ N_{0A_n} &\rightarrow N_{A_n} \end{aligned} \tag{25}$$

Also, $\phi_{\mathbf{A}} = (\phi_{A_1}, \phi_{A_2}, \dots, \phi_{A_n})$ and $\phi_{\mathbf{W}} = (\phi_{W_1}, \phi_{W_2}, \dots, \phi_{W_n})$ are linear operators such that $\phi_i(\alpha(t)) \rightarrow 0$ for any bounded $\alpha(t)$. Here, the effect of interference can be eliminated by designing the control system so that the interference term is equal to the feedback term, as shown in the following equation. Each operator is designed with $A_A = I$, $A_W = I$, $\phi_{A_i}^{-1}(\alpha_i)(t) = \frac{1}{n_a} \alpha_i$, $\phi_{W_i}^{-1}(\alpha_i)(t) = \frac{1}{n_w} \alpha_i$, where α_i is the bounded signal and n_a and n_w are design parameters.

$$\begin{aligned} z_i(t) &= u_{d_i} + d_i(t) + \phi_{A_i}^{-1} A_{A_i} \tilde{P}_{0A_i}(u_{d_i})(t) \\ &\quad + \phi_{W_i}^{-1} A_{W_i} \tilde{P}_{0W_i} \tilde{P}_{0A_i}(u_{d_i})(t) \\ &\quad - \phi_{A_i}^{-1} A_{A_i} \tilde{P}_{A_i}(z_i)(t) - \phi_{W_i}^{-1} A_{W_i} \tilde{P}_{W_i} \tilde{P}_{A_i}(z_i)(t) \end{aligned} \tag{26}$$

Transform the equation for $z_i(t)$.

$$\begin{aligned} &\phi_{A_i}^{-1}(\phi_{A_i} + A_{A_i} \tilde{P}_{A_i})(z_i)(t) + \phi_{W_i}^{-1}(\phi_{W_i} + A_{W_i} \tilde{P}_{W_i} \tilde{P}_{A_i})(z_i)(t) \\ &= d_i(t) + \phi_{A_i}^{-1}(\phi_{A_i} + A_{A_i} \tilde{P}_{0A_i})(u_{d_i})(t) \\ &\quad + \phi_{W_i}^{-1}(\phi_{W_i} + A_{W_i} \tilde{P}_{0W_i} \tilde{P}_{0A_i})(u_{d_i})(t) \end{aligned} \tag{27}$$

From the above equation, the input signal $z_i(t)$ equals the output $u_i(t)$ of operator B^{-1} .

$$z_i(t) \rightarrow u_{d_i}(t) \tag{28}$$

3.3. Controller Design

The control system designed based on operator theory is shown in Figure 3. In this case, each plant is $\mathbf{D}_{\mathbf{A}} = (D_{A_1}, D_{A_2}, \dots, D_{A_n})$, $\mathbf{N}_{\mathbf{A}} = (N_{A_1}, N_{A_2}, \dots, N_{A_n})$, and $\mathbf{P}_{\mathbf{W}} = (P_{W_1}, P_{W_2}, \dots, P_{W_n})$, and the controllers are $\mathbf{S} = (S_1, S_2, \dots, S_n)$, $\mathbf{R}_{\mathbf{W}} = (R_{W_1}, R_{W_2}, \dots, R_{W_n})$, and $\mathbf{C}_{\mathbf{W}} = (C_{W_1}, C_{W_2}, \dots, C_{W_n})$. Also, each signal is $\mathbf{e}^* = (e_1^*, e_2^*, \dots, e_n^*)$, $\mathbf{e} = (e_1, e_2, \dots, e_n)$, $\mathbf{r} = (r_1, r_2, \dots, r_n)$, $\mathbf{u}_{\mathbf{d}} = (u_{d_1}, u_{d_2}, \dots, u_{d_n})$, $\mathbf{w}_{\mathbf{a}} = (w_{a_1}, w_{a_2}, \dots, w_{a_n})$, $\mathbf{y}_{\mathbf{a}} = (y_{a_1}, y_{a_2}, \dots, y_{a_n})$, and $\mathbf{y} = (y_1, y_2, \dots, y_n)$. The nonlinear operator $\mathbf{N}_{\mathbf{A}} = (N_{A_1}, N_{A_2}, \dots, N_{A_n})$ for the thermal model of the aluminum block and the operator $\mathbf{P}_{\mathbf{W}} = (P_{W_1}, P_{W_2}, \dots, P_{W_n})$ for the thermal model of the tube are collectively denoted by $\tilde{\mathbf{N}}_{\mathbf{W}_n} = (\tilde{N}_{W_1}, \tilde{N}_{W_2}, \dots, \tilde{N}_{W_n})$, where the operators $\mathbf{S} = (S_1, S_2, \dots, S_n)$ and $\mathbf{R}_{\mathbf{W}} = (R_{W_1}, R_{W_2}, \dots, R_{W_n})$ are designed to satisfy the Bezout's identity shown in Equation (29). By designing stable operators S_n and R_{W_n} to satisfy Bezout's identity, D_{A_n} and \tilde{N}_{W_n} become right-irreducible and BIBO-stable in the feedback control system shown in Figure 3 [8].

$$S_n \tilde{N}_{W_n}(\omega_{a_n}) + R_{W_n} D_{A_n}(\omega_{a_n}) = I(\omega_{a_n}) \tag{29}$$

where I is the identity map. The operators designed with an arbitrary constant B_n are shown in Equations (30) and (31).

$$S_n(y_n) = (1 - B_n)(\tilde{N}_{W_n}^{-1}(y_n)) \tag{30}$$

$$R_{W_n}(u_{d_n}) = \frac{B_n}{m_a c_a} u_{d_n} \tag{31}$$

By designing as above, we obtain that

$$\begin{aligned}
 S_n \tilde{N}_{W_n}(\omega_{a_n}) + R_{W_n} D_{A_n}(\omega_{a_n}) &= (1 - B_n) \tilde{N}_{W_n}^{-1} \tilde{N}_{W_n}(\omega_{a_n}) + \frac{B_n}{m_a c_a} \times m_a c_a \omega_{a_n} \\
 &= (1 - B_n)(\omega_{a_n}) + B_n \omega_{a_n} \\
 &= \omega_{a_n} \\
 &= I(\omega_{a_n})
 \end{aligned}
 \tag{32}$$

and Equation (29) is satisfied. The tracking controller C_{W_n} designed to compensate for tracking performance is shown in Equation (33).

$$C_{W_n}(e_n) = K_{P_n} e_n + K_{I_n} \int_0^t e_n(\tau) d\tau
 \tag{33}$$

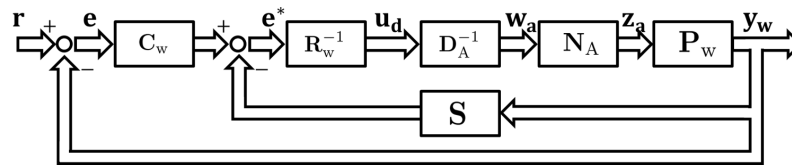


Figure 3. MIMO control system for microreactor based on operator theory.

3.4. Sensorless Control System with M-SVR

A sensorless control instrument using M-SVR is shown in Figure 4. The model for M-SVR was the model created in Section 2.3. y_{Mw} is the vector of temperatures of the microreactor estimated by M-SVR, and y_{Ma} is the vector of temperatures of the heat spreader estimated by M-SVR, y_{Ma_1} , y_{Ma_3} , combined with the measured value, y_{a_2} . H_1 is a controller that converts from heat to current and can be expressed as in Equation (34); H_2 is a controller that takes the temperature about the tube from the output of M-SVR and outputs the difference from the initial temperature; H_3 is a controller that takes the temperature about aluminum from the output of M-SVR and outputs the difference from the initial temperature. The parameters used are listed in Table 6.

$$H_1 : i = \begin{pmatrix} i_1 \\ i_2 \end{pmatrix} = \begin{pmatrix} \left(ST_{a_1} - \sqrt{(ST_{a_1})^2 - R(2K(T_0 - T_{a_1}) + 2u_{d_1})} \right) / R \\ \left(ST_{a_3} - \sqrt{(ST_{a_3})^2 - R(2K(T_0 - T_{a_3}) + 2u_{d_2})} \right) / R \end{pmatrix}
 \tag{34}$$

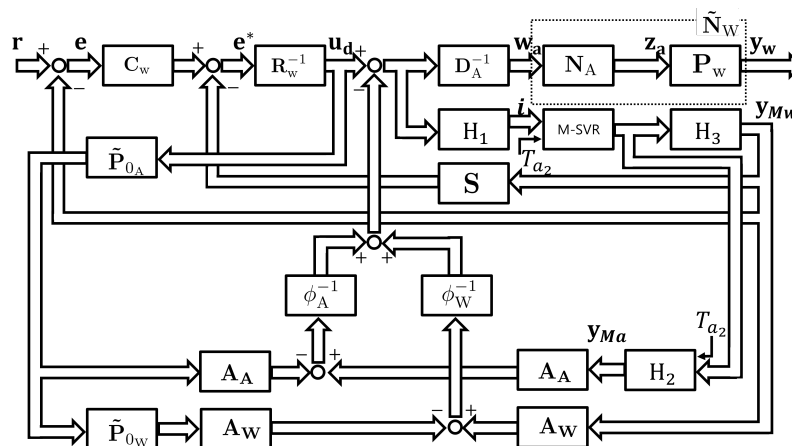


Figure 4. Proposed sensorless control system using M-SVR.

Table 6. Parameters of Peltier device.

Symbol	Description	Value	Unit
S	Seebeck coefficient	0.08	V/K
R	Electrical resistance	2	Ω
K	Thermal conductance	0.43	W/K

4. Simulation and Experiment

4.1. Experimental System

Figure 5 shows a diagram of the experimental apparatus. The experimental apparatus consists of a computer, power supply, microcomputer, temperature sensor circuit, current sensor circuit, and microreactor cooling block. The cooling block consists of a Peltier element, a heat spreader, a microreactor, and a fan. The microreactor and heat spreader are equipped with multiple temperature sensors. The operation flow of the system is shown below.

- Temperature acquisition**
 When the computer sends a command to the microcomputer to acquire the temperature, the microcomputer acquires the value from the temperature sensor circuit and sends the temperature value to the computer.
- Control input calculation and current value setting**
 Control inputs are calculated from operator theory based on target and acquisition temperatures. If necessary, the control input is converted to a current value. The calculated current value is sent to the microcomputer as a command current.
- Current control**
 The microcomputer performs PID control so that the current flowing through the Peltier element becomes the command current value received from the computer.
- Step 1 is repeated until the control time is reached.

Table 7 shows the common parameters used in the simulations and the actual experiments. A first-order low-pass filter with a cutoff frequency of 10 Hz was used for noise rejection in the actual experiment.

Table 7. Common parameters for simulation and experiment.

Symbol	Description	Value	Unit
T_s	Control time	500	s
Δt	Control cycle	1	s
B_{w_1}, B_{w_3}	Design parameter	0.999	–
n_{a_1}, n_{a_3}	Design parameter	1000	–
n_{w_1}, n_{w_3}	Design parameter	1000	–

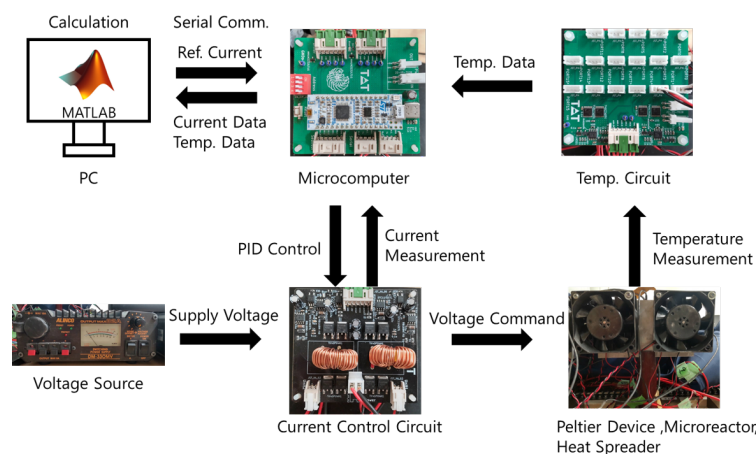


Figure 5. Diagram of the experimental apparatus.

4.2. Simulation Results for MIMO Control Systems

Figures 6 and 7 show the simulation results for the MIMO control system. The parameters used in the simulations are listed in Table 8. Figure 6 shows that T_{w_1} and T_{w_3} follow each other in about 150 s.

Table 8. Parameters for simulation.

Symbol	Description	Value	Unit
T_0	Initial temperature	28	°C
r_1	Reference of Part W_1	2.5	°C
r_2	Reference of Part W_3	2.3	°C
k_{p1}, k_{p3}	Proportional gain of Part W_1, W_3	0.02	–
k_{i1}, k_{i3}	Integral gain of Part W_1, W_3	0.00032	–

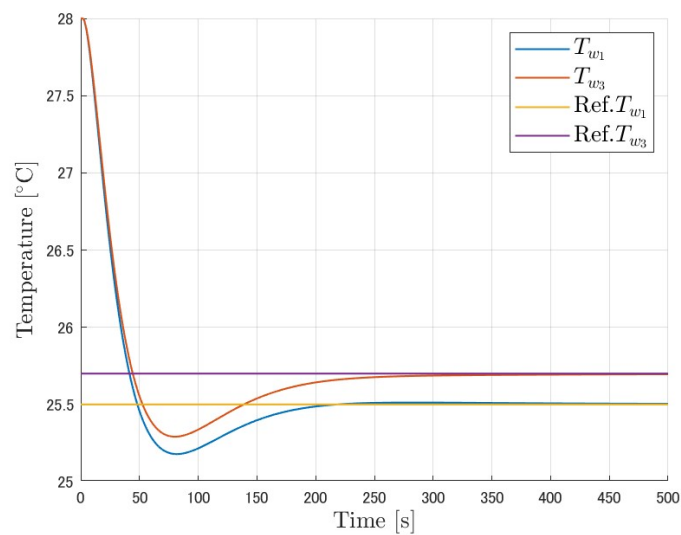


Figure 6. Microreactor temperature (simulation on MIMO control system).

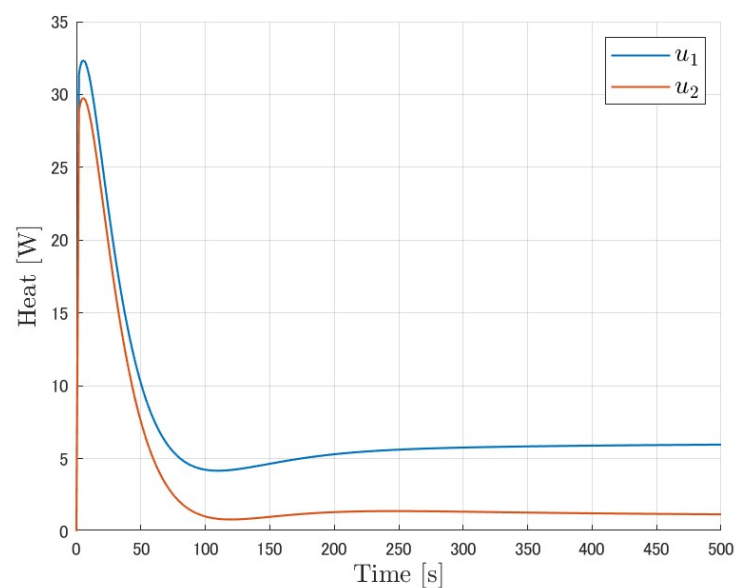


Figure 7. Control input (simulation on MIMO control system).

4.3. Results of Experiment

4.3.1. MIMO Control System

The experimental results of the MIMO control system are shown in Figures 8 and 9. Table 9 shows the parameters used in the experiments. Figure 8 shows that T_{w_1} and T_{w_3} follow each other in about 250 s.

Table 9. Parameters of experiment on MIMO control systems.

Symbol	Description	Value	Unit
T_0	Initial temperature	21.69	°C
r_1	Reference of Part W_1	2.0	°C
r_2	Reference of Part W_3	2.5	°C
k_{p_1}, k_{p_3}	Proportional gain of Part W_1, W_3	0.001	–
k_{i_1}, k_{i_3}	Integral gain of Part W_1, W_3	0.0002	–

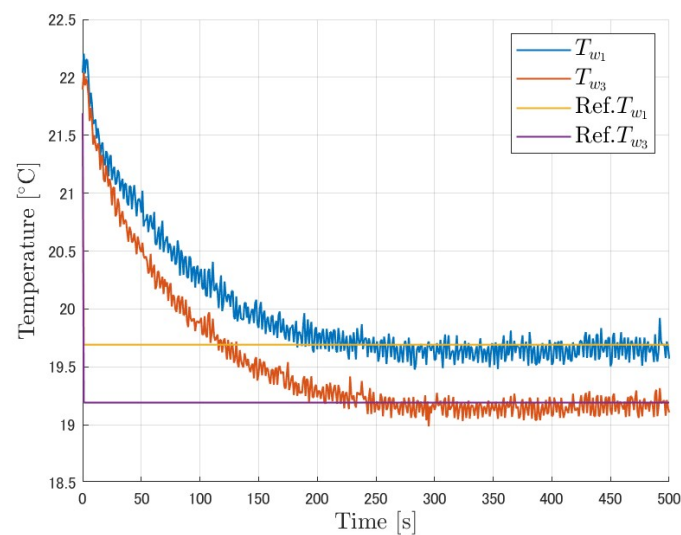


Figure 8. Microreactor temperature (experiment on MIMO control system).

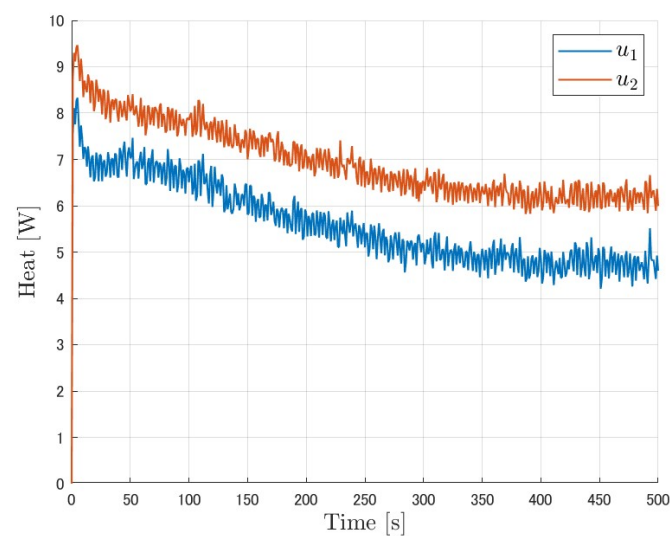


Figure 9. Control input (experiment on MIMO control system).

4.3.2. MIMO Sensorless Control Using M-SVR

Figures 10–12 show the experimental results of sensorless control using M-SVR. Table 10 shows the parameters used in the experiments. Here, T_{Mw_1} and T_{Mw_3} are the estimated values of M-SVR and are the signals used for feedback, while T_{w_1} and T_{w_3} are only measurements and are not used for control. Figures 10 and 11 show that the estimated values of T_{Mw_1} and T_{Mw_3} of M-SVR follow each other in about 320 s.

Table 10. Parameters of experiment on MIMO sensorless control using M-SVR.

Symbol	Description	Value	Unit
T_0	Initial temperature	27.68	°C
r_1	Reference of Part W_1	2.7	°C
r_2	Reference of Part W_3	2.5	°C
k_{p_1}, k_{p_3}	Proportional gain of Part W_1, W_3	0.001	–
k_{i_1}, k_{i_3}	Integral gain of Part W_1, W_3	0.0002	–

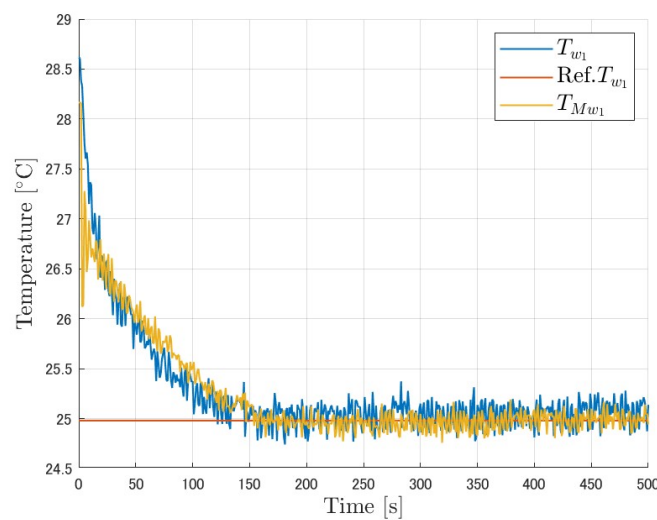


Figure 10. Microreactor temperature T_{w_1} and M-SVR estimate T_{Mw_1} (experiment).

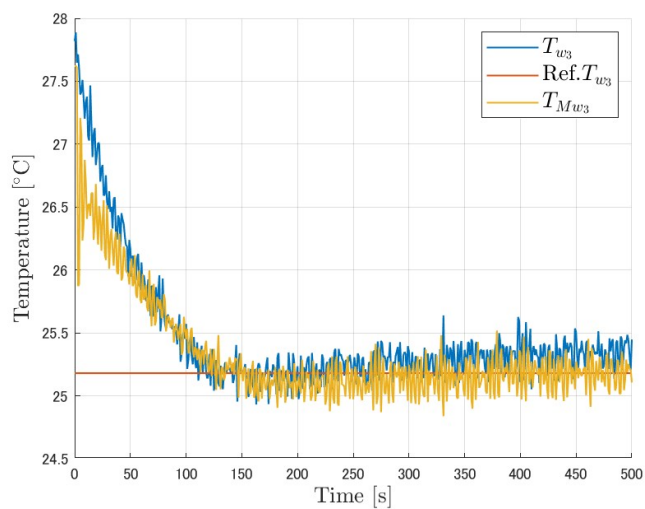


Figure 11. Microreactor temperature T_{w_3} and M-SVR estimate T_{Mw_3} (experiment).

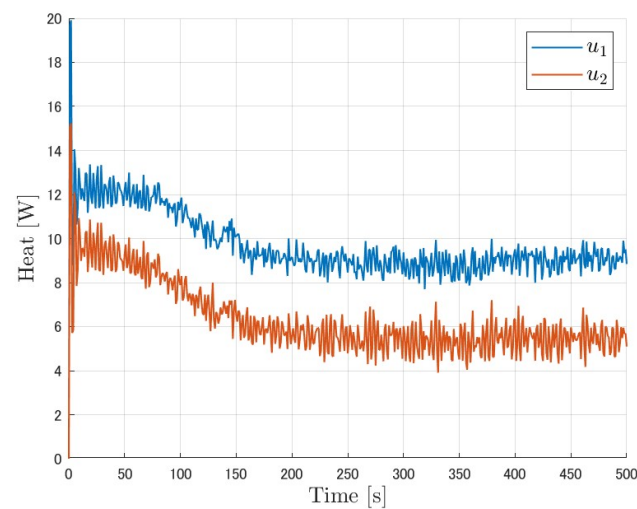


Figure 12. Control input (experiment on MIMO sensorless control using M-SVR).

4.4. Discussion

Compare Figures 6 and 7, which are simulation results of the control system in Figures 3, 8 and 9, which are the results of actual machine experiments. Figure 9, which is a graph of temperature, shows an overshoot, whereas Figure 8 does not. In addition, the simulation results show a faster target value tracking time than the experimental results. This is due to the fact that the heat spreader used in the experimental system has a cavity, which has a smaller thermal conductivity than in reality. And, even though the difference between the two cooling temperatures is larger in the actual experiment than in the simulation, the simulation results are more biased than Figures 7 and 9. The reason for this is that the heat spreader used in the experimental system has a cavity, which is not taken into account, and therefore the thermal conductivity of the model is larger than in reality. From Figures 10 and 11, which are the results of the sensorless control system using M-SVR, it can be seen that there are errors between the sensor values and the estimated values. This is due to modeling errors that occur when the model is created via M-SVR.

5. Conclusions

In this study, a MIMO temperature control system for a microreactor was designed and its effectiveness was confirmed through simulations and experiments. The proposed method can control two temperatures in a microreactor, whereas the conventional method can control only one temperature in a microreactor, thus allowing for a high degree of freedom in temperature control. We also created a machine learning model of the M-SVR of a microreactor using a generalized Gaussian kernel and conducted actual experiments on sensorless control using the model to confirm its effectiveness. The hyperparameters of the M-SVR were optimized using a real-coded genetic algorithm, one of the metaheuristics, and then adjusted manually. The MSE of each output was lower for the generalized Gaussian kernel than for the RBF kernel, indicating the accuracy of the model. In addition, the fact that the M-SVR estimates from the experiment are distributed near the corresponding sensor values confirms that they are correctly estimated and confirms the effectiveness of sensorless control.

Author Contributions: T.K. applied a generalized Gaussian kernel as the kernel function of M-SVR and performed parameter optimization using a real-coded genetic algorithm. Using the model, a sensorless control of a MIMO temperature control system of a microreactor was proposed. In addition, K.N. proposed a method to extend the temperature control system of a microreactor to a MIMO temperature control system, and M.D. suggested technical support and gave overall guidance on the paper. All authors have read and agreed to the published version of the manuscript.

Funding: This research received no external funding.

Institutional Review Board Statement: Not applicable.

Informed Consent Statement: Not applicable.

Data Availability Statement: Data are contained within the article.

Conflicts of Interest: The authors declare no conflicts of interest.

Abbreviations

The following abbreviations are used in this manuscript:

- MIMO Multi-input multi-output
- M-SVR Multi-output support vector regression
- MSE Mean square error

Appendix A. Separation of Coupling Elements

When performing MIMO temperature control, it is necessary to consider the coupling elements that occur between each control system. In this study, the coupling elements are separated based on Reference [8], and the two-input, two-output control system is divided into two independent subsystems for control. Figure A1 shows a MIMO system plant with coupling elements. Here, U is the input space, V is the output space, and $\mathbf{u} = (u_1, u_2, \dots, u_n), \mathbf{y} = (y_1, y_2, \dots, y_n)$ are the inputs and outputs of the nominal plant $\mathbf{P} = (P_1, P_2, \dots, P_n): U \rightarrow V$. The operator $\mathbf{N} = (N_1, N_2, \dots, N_n): W \rightarrow V$ is nonlinear and stable, and \mathbf{P} is diagonalizable. The plant can then undergo right factorization as follows.

$$\mathbf{P} = \mathbf{N}\tilde{\mathbf{D}}^{-1} \tag{A1}$$

where \mathbf{D} is linear, stable and invertible. We define the operator \mathbf{F} with respect to the coupling elements, as in the following equation, where \mathbf{f} is a bounded unknown.

$$\begin{aligned} \mathbf{v}(t) &= \mathbf{F}(\mathbf{w})(t) = \mathbf{F} \cdot \mathbf{w}(t) + \mathbf{f}(t) \\ \mathbf{w} &= (w_1, w_2, \dots, w_n) \in W \\ \mathbf{v} &= (v_1, v_2, \dots, v_n) \in W \\ \mathbf{f} &= (f_1, f_2, \dots, f_n) \in W \end{aligned} \tag{A2}$$

In this case, $\tilde{\mathbf{D}}$ can be expressed as follows:

$$\tilde{\mathbf{D}} = \mathbf{D}\mathbf{F} : W \rightarrow U \tag{A3}$$

Next, consider a MIMO system with feedback signals as shown in Figure A2, where \mathbf{S} is the feedback operator and b is the feedback signal $\mathbf{b} = \mathbf{S}(\mathbf{y})$.

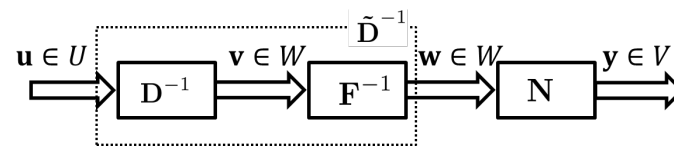


Figure A1. MIMO system plant.

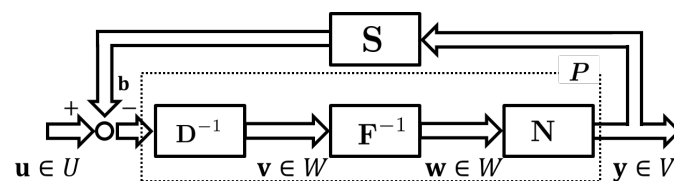


Figure A2. MIMO system stabilization via operator theory.

Each element b_i of the feedback signal b is expressed by the following equation, which includes the coupling elements.

$$b_i = \sum_{j=i}^n S_{ij}(y_j) \tag{A4}$$

However, the coupling factor can be eliminated by designing the operator to satisfy the following equation.

$$S_{ij}N_j + F_{ij}D_i = \begin{cases} 0, & j \neq i \\ R_i, & j = i \end{cases} \tag{A5}$$

In this case, the coupling factor is removed from the input u as in the following equation, which can be converted to an equation including the disturbances f and ω .

$$u_i(t) = D_i(v_i) + \sum_{j=i}^n S_{ij}(y_j)(t) \tag{A6}$$

$$= D_i(f_i) + \sum_{j=i}^n (S_{ij}N_j + D_iF_{ij})(\omega_j)(t) \tag{A7}$$

$$= D_i(f_i) + R_i(\omega_i)(t) \tag{A8}$$

The right factorization can then be transformed as follows.

$$\tilde{P}_i = N_iR_i^{-1} \tag{A9}$$

Appendix B. M-SVR

M-SVR (Multi-output Support Vector Regression) is an SVR for multi-output problems and is a regression analysis method that can take into account the effects among outputs [28,29]. Consider the case of d input ($\mathbf{x} \in \mathbb{R}^d$) and Q output ($\mathbf{y} \in \mathbb{R}^Q$). Assuming $j = 1, 2, \dots, Q$, the j th coefficient vector is $\mathbf{w}^j \in \mathbb{R}^d$ and the bias is $b^j \in \mathbb{R}$, the regression equation f becomes Equation (A10).

$$f^j(\mathbf{x}) = (\mathbf{w}^j)^\top \mathbf{x} + b^j \tag{A10}$$

Let $\mathbf{f}(\mathbf{x}) = [f^1(\mathbf{x}), f^2(\mathbf{x}), \dots, f^Q(\mathbf{x})]^\top \in \mathbb{R}^Q$, $\mathbf{W} = [\mathbf{w}^1, \mathbf{w}^2, \dots, \mathbf{w}^Q] \in \mathbb{R}^{d \times Q}$, $\mathbf{b} = [b^1, b^2, \dots, b^Q]^\top \in \mathbb{R}^Q$, and $\phi(\mathbf{x})$ be a function $\phi(\mathbf{x}) : \mathbb{R}^d \rightarrow F$ that maps the input \mathbf{x} to the feature space F . The regression equation for M-SVR is Equation (A11).

$$\mathbf{f}(\mathbf{x}) = \mathbf{W}^\top \phi(\mathbf{x}) + \mathbf{b} \tag{A11}$$

Let $\mathbf{e}_i = \mathbf{y}_i - \mathbf{f}(\mathbf{x}_i)$ and $u_i = \|\mathbf{e}_i\| = \sqrt{\mathbf{e}_i^\top \mathbf{e}_i}$, and define the cost function $L_p(\mathbf{W}, \mathbf{b})$ and the loss function $L(u)$ as Equations (A12) and (A13).

$$L_p(\mathbf{W}, \mathbf{b}) = \frac{1}{2} \sum_{j=1}^Q \|\mathbf{w}^j\|^2 + C \sum_{i=1}^l L(u_i) \tag{A12}$$

$$L(u) = \begin{cases} 0 & u < \epsilon \\ u^2 - 2u\epsilon + \epsilon^2 & u \geq \epsilon \end{cases} \tag{A13}$$

C is the regularization factor and ϵ is the insensitivity parameter. The M-SVR used in this study determines the parameters of the optimal regression equation using a type of

iterative method called IRWLS (Iterative Reweighted Least Square). To construct IRWLS, Equation (A12) is first-order Taylor-expanded.

$$L'_P(\mathbf{W}, \mathbf{b}) = \frac{1}{2} \sum_{j=1}^Q \|w^j\|^2 + C \left(\sum_{i=1}^n L(u_i^k) + \frac{dL(u)}{du} \Big|_{u_i^k} \frac{(\mathbf{e}_i^k)^\top}{u_i^k} [\mathbf{e}_i - \mathbf{e}_i^k] \right) \tag{A14}$$

where $u_i^k = \|\mathbf{e}_i^k\| = \sqrt{(\mathbf{e}_i^k)^\top \mathbf{e}_i^k}$, $(\mathbf{e}_i^k)^\top = \mathbf{y}_i^\top - \boldsymbol{\phi}^\top(\mathbf{x}_i) \mathbf{W}^k - (\mathbf{b}^k)^\top$.

This is the quadratic approximation of Equation (A14).

$$L''_P(\mathbf{W}, \mathbf{b}) = \frac{1}{2} \sum_{j=1}^Q \|w^j\|^2 + C \left(\sum_{i=1}^n L(u_i^k) + \frac{dL(u)}{du} \Big|_{u_i^k} \frac{u_i^2 - (u_i^k)^2}{2u_i^k} \right) \tag{A15}$$

$$= \frac{1}{2} \sum_{j=1}^Q \|w^j\|^2 + \frac{1}{2} \sum_{i=1}^n a_i u_i^2 + CT \tag{A16}$$

a_i can be expressed as in Equation (A17).

$$a_i = \frac{C}{u_i^k} \frac{dL(u)}{du} \Big|_{u_i^k} = \begin{cases} 0 & u_i^k < \epsilon \\ \frac{2C(u_i^k - \epsilon)}{u_i^k} & u_i^k \geq \epsilon \end{cases} \tag{A17}$$

In addition, CT is a term that represents the sum of constants and does not depend on \mathbf{W} or \mathbf{b} . The IRWLS algorithm is shown below.

1. Initialize $k = 0$, $\mathbf{W}^k = \mathbf{0}$, $\mathbf{b}^k = \mathbf{0}$, and compute u_i^k and a_i .
2. Equation (A16) is calculated and the obtained \mathbf{W} and \mathbf{b} are defined as \mathbf{W}_s and \mathbf{b}_s . The decreasing direction \mathbf{P} in Equation (A12) is defined as Equation (A18).

$$\mathbf{P} = \begin{bmatrix} \mathbf{W}^s - \mathbf{W}^k \\ (\mathbf{b}^s - \mathbf{b}^k)^\top \end{bmatrix} \tag{A18}$$

3. The solution of the next step is obtained from Equation (3). η^k is calculated via a backtracking algorithm.

$$\begin{bmatrix} \mathbf{W}^{k+1} \\ (\mathbf{b}^{k+1})^\top \end{bmatrix} = \begin{bmatrix} \mathbf{W}^k \\ (\mathbf{b}^k)^\top \end{bmatrix} + \eta^k \mathbf{P}^k \tag{A19}$$

4. Compute u_i^k, a_i . Return to 2 until convergence.

In the following, we will address how to obtain W_s and b_s . To obtain W_s and b_s , it is necessary to solve the weighted least-squares problem in Equation (A16). Then, by partial differentiation of Equation (A16) with w^j and b^j , and setting their slopes to zero, Equations (A20) and (A21) are obtained.

$$\nabla_{w^j} L_P'' = w^j - \sum_i \phi(x_i) a_i (y_{ij} - \phi^\top(x_i) w^j - b^j) = 0 \tag{A20}$$

$$\nabla_{b^j} L_P'' = - \sum_i a_i (y_{ij} - \phi^\top(x_i) w^j - b^j) = 0 \tag{A21}$$

where $\mathbf{0} \in \mathbb{R}^d$. Equations (A20) and (A21) can be expressed in matrix notation as in Equation (A22).

$$\begin{bmatrix} \Phi^\top D_a \Phi + I & \Phi^\top a \\ a^\top \Phi & \mathbf{1}^\top a \end{bmatrix} \begin{bmatrix} w^j \\ b^j \end{bmatrix} = \begin{bmatrix} \Phi^\top D_a y^j \\ a^\top y^j \end{bmatrix} \tag{A22}$$

where $\Phi = [\phi(x_1), \dots, \phi(x_n)]^\top \in \mathbb{R}^{d \times n}$, $a = [a_1, \dots, a_n]^\top \in \mathbb{R}^n$, $y^j = [y_{1j}, \dots, y_{nj}]^\top \in \mathbb{R}^n$, $D = \text{diag}(a) \in \mathbb{R}^{n \times n}$ and $\mathbf{1} \in \mathbb{R}^n$.

Next, a feature space kernel is introduced to accommodate nonlinearities. Substituting the Representer Theorem $w^j = \sum_i \phi(x_i) \beta^j = \Phi^\top \beta^j$ into Equations (A20) and (A21), we obtain Equation (A23).

$$\begin{bmatrix} K + D_a^{-1} & \mathbf{1} \\ a^\top K & \mathbf{1}^\top a \end{bmatrix} \begin{bmatrix} \beta^j \\ b^j \end{bmatrix} = \begin{bmatrix} y^j \\ a^\top y^j \end{bmatrix} \tag{A23}$$

where $(K)_{ij} = \kappa(x_i, x_j)$. By changing $W^s \beta^s$ to $W^k \beta^k$ and W^k to β^k in the IRWLS algorithm described earlier, nonlinear multiple-output support vector regression can be realized.

Appendix C. Generalized Gaussian Kernel

The generalized Gaussian kernel is a kernel based on a generalized Gaussian distribution [27]. Equation (A24) shows the generalized Gaussian function.

$$f(x) = \frac{g(\gamma)\gamma}{2\sigma\Gamma(1/\gamma)} \exp\left[-\left(\frac{g(\gamma)\|x - \mu e\|}{\sigma}\right)^\gamma\right] \tag{A24}$$

$$g(\gamma) = \sqrt{\frac{\Gamma(3/\gamma)}{\Gamma(1/\gamma)}} \tag{A25}$$

$x \in \mathbb{R}^n$ is the input, μ is the mean, σ is the standard deviation, γ is the shape parameter, $e \in \mathbb{R}^n$ is the unit vector, and $\Gamma(z)$ is the gamma function. The shape parameter is also called the decay ratio because a smaller value of the shape parameter γ results in a sharper probability density function, while a larger value results in a flatter probability density function.

Based on the above, the generalized Gaussian kernel is shown in Equation (A26).

$$f(x_i, x_j) = \frac{g(\gamma)\gamma}{2\sigma\Gamma(1/\gamma)} \exp\left(-\left(\frac{g(\gamma)\|x_i - x_j\|}{\sigma}\right)^\gamma\right) \tag{A26}$$

References

1. Hinterleitner, B.; Knapp, I.; Poneder, M.; Shi, Y.; Müller, H.; Eguchi, G.; Eisenmenger-Sittner, C.; Stöger-Pollach, M.; Kakefuda, Y.; Kawamoto, N.; et al. Thermoelectric performance of a metastable thin-film Heusler alloy. *Nature* **2019**, *576*, 85–90. [[CrossRef](#)] [[PubMed](#)]
2. Zhao, D.; Tan, G. A review of thermoelectric cooling: Materials, modeling and applications. *Appl. Therm. Eng.* **2014**, *66*, 15–24. [[CrossRef](#)]
3. Deng, M.; Iwai, Z.; Mizumoto, I. Robust parallel compensator design for output feedback stabilization of plants with structured uncertainty. *Syst. Control Lett.* **1999**, *36*, 193–198. [[CrossRef](#)]
4. Rsetam, K.; Cao, Z.; Man, Z. Design of Robust Terminal Sliding Mode Control for Underactuated Flexible Joint Robot. *IEEE Trans. Syst. Man Cybern. Syst.* **2022**, *52*, 4272–4285. [[CrossRef](#)]
5. Man, Z.; Paplinski, A.P.; Wu, H. A robust MIMO terminal sliding mode control for rigid robotic manipulators. *IEEE Trans. Autom. Control* **1994**, *39*, 2264–2469.
6. Wang, H.; Man, Z.; Kong, H.; Zhao, Y.; Yu, M.; Cao, Z.; Zheng, J.; Do, M.T. Design and Implementation of Adaptive Terminal Sliding-Mode Control on a Steer-by-Wire Equipped Road Vehicle. *IEEE Trans. Ind. Electron.* **2016**, *63*, 5774–5785. [[CrossRef](#)]
7. Yu, X.; Man, Z. Model reference adaptive control systems with terminal sliding modes. *Int. J. Control* **1996**, *64*, 1165–1176. [[CrossRef](#)]
8. Deng, M. Robust Stability of Operator-Based Nonlinear Control Systems. In *Operator-Based Nonlinear Control Systems: Design and Applications*; John Wiley & Sons, Ltd.: Hoboken, NJ, USA, 2014; pp. 27–115.
9. Chen, G.; Han, Z. Robust right coprime factorization and robust stabilization of nonlinear feedback control systems. *IEEE Trans. Autom. Control* **1998**, *43*, 1505–1509. [[CrossRef](#)]
10. Deng, M.; Inoue, A.; Goto, S. Operator based Thermal Control of an Aluminum Plate with a Peltier Device. *Int. J. Innov. Comput. Inf. Control* **2008**, *4*, 3219–3229.
11. Matsui, A.; Meng, L.; Hattori, K. Enhanced YOLO using Attention for Apple grading. In Proceedings of the 2023 International Conference on Advanced Mechatronic Systems (ICAMEchS), Melbourne, Australia, 4–7 September 2023.
12. Li, Z.; Meng, L. Research on Deep Learning-based Cross-disciplinary Applications. In Proceedings of the 2022 International Conference on Advanced Mechatronic Systems (ICAMEchS), Toyama, Japan, 17–20 December 2022.
13. Atsumi, M.; Kawano, S.; Morioka, T.; Meng, L. Deep Learning Based Ancient Asian Character Recognition. In Proceedings of the 2020 International Conference on Advanced Mechatronic Systems (ICAMEchS), Hanoi, Vietnam, 10–13 December 2020.
14. Zhang, Y.; Meng, L.; Xue, X.; Zhou, Z.; Tomiyama, H. QoE-Constrained Concurrent Request Optimization through Collaboration of Edge Servers. *IEEE Internet Things J.* **2019**, *6*, 9951–9962. [[CrossRef](#)]
15. Meng, L.; Hirayama, T.; Oyanagi, S. Underwater-Drone with Panoramic Camera for Automatic Fish Recognition Based on Deep Learning. *IEEE Access* **2018**, *6*, 17880–17886. [[CrossRef](#)]
16. Chen, L.; Li, X.; Ma, L.; Bi, S. Probabilistic neural network based apple classification prediction. In Proceedings of the 2022 International Conference on Advanced Mechatronic Systems (ICAMEchS), Toyama, Japan, 17–20 December 2022.
17. Bi, S.; Qu, X.; Ma, L.; Shen, T.; Han, C. Apple Grading Method Based on Ordered Partition Neural Network. In Proceedings of the 2021 International Conference on Advanced Mechatronic Systems (ICAMEchS), Tokyo, Japan, 9–12 December 2021.
18. Wang, C.; Man, Z.; Jin, J.; Ye, W. Hash-Based Convolutional Deep-thinking Pattern Classifier. In Proceedings of the 2023 International Conference on Advanced Mechatronic Systems (ICAMEchS), Melbourne, Australia, 4–7 September 2023.
19. Gao, X.; Yang, Q.; Zhang, J. Multi-objective optimisation for operator-based robust nonlinear control design for wireless power transfer systems. *Int. J. Adv. Mechatron. Syst.* **2022**, *9*, 203–210. [[CrossRef](#)]
20. Zhang, Z.; Wen, F.; Shi, J.; He, J.; Truong, T.-K. 2D-DOA Estimation for Coherent Signals via a Polarized Uniform Rectangular Array. *IEEE Signal Process. Lett.* **2023**, *30*, 893–897. [[CrossRef](#)]
21. Usami, T.; Deng, M. Applying an MSVR Method to Forecast a Three-Degree-of-Freedom Soft Actuator for a Nonlinear Position Control System: Simulation and Experiments. *IEEE Syst. Man Cybern. Mag.* **2022**, *8*, 61–69. [[CrossRef](#)]
22. Bu, N.; Zhang, Y.; Li, X. Robust tracking control for uncertain micro-hand actuator with Prandtl-Ishlinskii hysteresis. *Int. J. Robust Nonlinear Control* **2023**, *33*, 9391–9405. [[CrossRef](#)]
23. Bu, N.; Liu, H.; Li, W. Robust passive tracking control for an uncertain soft actuator using robust right coprime factorization. *Int. J. Robust Nonlinear Control* **2021**, *31*, 6810–6825. [[CrossRef](#)]
24. Bu, N.; Wang, X. Swing-up design of double inverted pendulum by using passive control method based on operator theory. *Int. J. Adv. Mechatron. Syst.* **2022**, *1*, 1. [[CrossRef](#)]
25. An, Z.; Bu, N. Modeling for a Bellow-Shaped Soft Actuator Based on Yeoh model and Operator-Based Nonlinear Control Design. In Proceedings of the 2023 International Conference on Advanced Mechatronic Systems (ICAMEchS), Melbourne, Australia, 4–7 September 2023.
26. Deng, M.; Saijo, N.; Gomi, H.; Inoue, A. A robust real time method for estimating human multijoint arm viscoelasticity. *Int. J. Innov. Comput. Inf. Control* **2006**, *2*, 705–721.
27. Deng, M.; Inoue, A.; Zhu, Q.M. An integrated study procedure on real-time estimation of time-varying multi-joint human arm viscoelasticity. *Trans. Inst. Meas. Control* **2011**, *33*, 919–941. [[CrossRef](#)]
28. Sanchez-Fernandez, M.; de-Prado-Cumplido, M.; Arenas-Garcia, J.; Arenas-Garcia, F. SVM multiregression for nonlinear channel estimation in multiple-input multiple-output systems. *IEEE Trans. Signal Process.* **2004**, *52*, 2298–2307. [[CrossRef](#)]

29. Tuia, D.; Verrelst, J.; Alonso, L.; Perez-Cruz, F.; Camps-Valls, G. Multioutput Support Vector Regression for Remote Sensing Biophysical Parameter Estimation. *IEEE Geosci. Remote Sens. Lett.* **2011**, *8*, 804–808. [[CrossRef](#)]
30. Ono, I.; Kita, H.; Kobayashi, A. A Real-coded Genetic Algorithm using the Unimodal Normal Distribution Crossover. In *Advances in Evolutionary Computing: Theory and Applications*; Ghosh, A., Tsutsui, S., Eds.; Springer: Berlin/Heidelberg, Germany, 2003; pp. 213–237.
31. Tsutsui, S.; Yamamura, M.; Higuchi, T. Multi-parent recombination with simplex crossover in real coded genetic algorithms. In *Proceedings of the 1st Annual Conference on Genetic and Evolutionary Computation—Volume 1, Orlando, FL, USA, 13–17 July 1999*.

Disclaimer/Publisher’s Note: The statements, opinions and data contained in all publications are solely those of the individual author(s) and contributor(s) and not of MDPI and/or the editor(s). MDPI and/or the editor(s) disclaim responsibility for any injury to people or property resulting from any ideas, methods, instructions or products referred to in the content.